JOURNAL OF OPTOELECTRONICS AND ADVANCED MATERIALS, Vol. 10, No. 9, September 2008, p. 2244 - 2251

Preparation and structural characterization by XRD and XAS of the supported gold catalysts

M. LAZAR[a], V. ALMASAN[a], S.PINTEA[a], B. BARZ[b*], C. DUCU[c], V. MALINOVSCHI[c], X. YANING[d], N. ALDEA[a**]
[a] *National Institute for Research and Development of Isotopic and Molecular Technologies, P. O. Box 700, 400293Cluj-Napoca, Romania,*
[b]*University of Missouri- Columbia, 223 Physics Building, MO 65211, USA*
[c]*University of Pitesti, Advanced Materials Department, Romania.*
[d]*Coordination Laboratory of National Center for Nanoscience and Nanotechnology, Synchrotron Radiation Facilities of Beijing Electron Positron Collider, People's Republic of China*

A series of supported gold catalysts were studied by X-ray diffraction (XRD) in order to determine the Au average particle size, microstrain information and probability of faults. The gold catalysts samples (up to 5 wt.% gold content) were prepared by two methods - impregnation of the oxidic support with aqueous solution of $HAuCl_4.3H_2O$ and homogeneous deposition-precipitation using urea as precipitating agent. The following metal oxides, with high specific surface area were used as supports: Cr_2O_3, CeO_2, TiO_2, SiO_2, Al_2O_3 and ZrO_2. The XRD method is based on the deconvolution of the experimental X-ray line profiles (XRLP) (111), (200), (220) and (311) using Fourier transform procedure. The global structure is determined by fitting the XRLP with the generalized Fermi function. The X-ray diffraction data was collected at room temperature, using Bragg-Brentano (BB) geometry installed on DRON 2 set up, connected with a PC. The samples were next analyzed by extended X-ray absorption fine structure (EXAFS) of the Au L_{III}-edge using synchrotron radiation in order to determine their local structure that explains the strong deformation of the metal due to its interaction with the oxide supports.

(Received February 25, 2008; accepted August 14, 2008)

Keywords: supported gold catalysts, local and global structure, metal support interaction, X-ray diffraction, synchrotron radiation

1. Introduction

Pure gold was considered for a long time an uninteresting metal from the point of view of catalysis. However, relatively recently it was reported to be extremely active for some reactions such as oxidation, reduction, isotopic exchange and hydrogenation if deposited as nanoparticles on different oxide supports [1-4]. We have studied in several papers the gold nanostructures [5-7]. In this paper we present the influence of the preparation method and oxide support nature on the structural properties of the gold based catalysts, determined by X ray diffraction (XRD) and X ray Absorption Spectroscopy (XAS) techniques. Theoretical aspects of these techniques are presented along with their direct application in determining the local and global structure of gold nanoparticles. This structure explains the strong interaction of the nanoparticles with the oxide support and the reactant at the electronic level. The modification of interface electronic properties due to this interaction has an important role in the creation of active centres on gold surfaces.

2. Theoretical background

2.1 EXAFS analysis

The interference between the outgoing and the backscattered electron waves has the effect of modulating the X-ray absorption coefficient. The EXAFS function $\chi(k)$ is defined in terms of the atomic absorption coefficient

$$\chi(k) = \frac{\mu(k) - \mu_0(k)}{\mu_0(k)}, \qquad (1)$$

where k is the electron wave vector, $\mu(k)$ refers to the absorption by an atom from the material of interest and $\mu_0(k)$ refers to the atom in the free state. EXAFS theories based on single scattering approximation of the ejected photoelectron by atoms in the immediate vicinity of the absorbing atom give the following expression [5] for $\chi(k)$

$$\chi(k) = \sum_j A_j(k) \sin\left[2kr_j + \delta_j(k)\right] \qquad (2)$$

where the summation extends over j coordination shell, r_j is the radial distance from the jth shell and $\delta_j(k)$ is the total phase shift function. The amplitude function $A_j(k)$ is given by

$$A_j(k) = \left(\frac{N_j}{kr_j}\right) F(k, r_j, \pi) \exp\left[-2(r_j/\lambda_j(k) - k^2\sigma_j^2)\right] \qquad (3)$$

In expression (3) N_j is the number of atoms in the *j*th shell, σ_j is the root mean square deviation of the distance about r_j, $F(k,r,\pi)$ is the backscattering amplitude and $\lambda_j(k)$ is the mean free path function for inelastic scattering. The backscattering factor and the phase shift depend on the type of atom responsible for scattering and its coordination shell [9]. The analysis of EXAFS data for obtaining structural information [N_j, r_j, σ_j, $\lambda(k)$] is generally done by the use of the Fourier transform. In this way, the radial structure function can be derived from $\chi(k)$ and the single shell may be isolated as follows

$$\Phi(r) = \int_{-\infty}^{\infty} k^n \chi(k) WF(k) \exp(-2ikr) dk . \qquad (4)$$

The EXAFS signal is weighted by k^n ($n=1, 2, 3...$) to get the reliable distribution function of atom distances. Different filtering windows $WF(k)$ are available as Kaiser or Hanning distributions. An inverse Fourier transform of the RSF can be obtained for any coordination shell,

$$\chi_j(k) = \left(1/k^n\right) WF(k) \int_{R_{1j}}^{R_{2j}} \Phi(r) \exp(2ikr)\, dr \cdot \qquad (5)$$

The theoretical equation for $\chi_j(k)$ function is given by:

$$\chi_j(k) = A_j(k) \sin\left[2kr_j + \delta_j(k)\right], \qquad (6)$$

where the index *j* refers to the *j*th coordination shell. The structural parameters for the first coordination shell are determined by fitting the $\chi_j(k)$ function derived from eq. (5) with the theoretical function $\chi_j(k)$ in eq. (6). In empirical EXAFS calculation, $F(k,r,\pi)$, $\lambda(k)$ and $\delta_j(k)$ are conveniently parameterized [10-13]. Ten coefficients are introduced for each shell:

$$\mathrm{F_s(k,r,\pi) = c_0\left[\exp(c_1 k + c_2 k^2)\right] / k^{c_3}} \qquad (7)$$

$$\delta_s(k) = a_{-1}k^{-1} + a_0 + a_1 k + a_2 k^2 \qquad (8)$$

$$\lambda(k) = \frac{1}{\Gamma}\left[k + \left(\frac{\eta}{k}\right)^4\right] \qquad (9)$$

The coefficients c_0, c_1, c_2, c_3, a_{-1}, a_0, a_1, a_2 are derived from the EXAFS spectrum of a compound whose structure is accurately known. The values N_s and r_s of each coordination shell for standard sample are known. The trial values of the eight coefficients can be analytically calculated and then varied until the fit between the observed and calculated EXAFS is optimized. The mean free path parameters are obtained during the fit procedure for each coordination shell.

2.2 XRD analysis

The X-ray diffraction pattern of a crystal can be described in terms of scattering intensity as a function of the scattering direction defined by the scattering angle 2θ, or by the scattering parameter $s = \frac{2\sin\theta}{\lambda}$, where λ is wavelength of the incident radiation. Next we shall discuss the X-ray diffraction theory applied to a mosaic structure model in which the atoms are arranged in blocks, each block itself being an ideal crystal. However, adjacent blocks do not accurately fit together. The experimental XRLP, *h*, represents the convolution between the true sample *f* and the instrumental function *g*:

$$h(s) = \int g(s - s^*) f(s^*)\, ds^* \qquad (10)$$

The eq. (9) is equivalent with the following relation

$$H(L) = G(L)F(L), \qquad (11)$$

where $F(L)$, $H(L)$ and $G(L)$ are Fourier transforms (FT) of the true sample, experimental XRLP and instrumental function. The variable *L* is the perpendicular vector to the (hkl) reflection planes. The normalized $F(L)$ can be described as the product of two factors, $F^{(s)}(L)$ and $F^{(\varepsilon)}(L)$. The factor $F^{(s)}(L)$ describes the contribution of crystallite size and stocking fault probability while the factor $F^{(\varepsilon)}(L)$ gives information about the microstrain of the lattice. Based on Warren and Averbach theory, the general form of the Fourier transform of the true sample for cubic lattices is given by relation,

$$F^{(s)}(L) = e^{-\frac{|L|}{D_{eff}(hkl)}},$$

$$F^{(\varepsilon)}(L) = e^{-\frac{2\pi^2 \left\langle \varepsilon_L^2 \right\rangle_{hkl} h_0^2 L^2}{a^2}}, \qquad (12)$$

where $D_{eff}(hkl)$ is the effective crystallite size, $\langle\varepsilon^2\rangle_{hkl}$ is the microstrain of the lattice and $h_0^2 = h^2 + k^2 + l^2$.

Approximate relations of the effective crystallite size and microstrain corresponding to small values of L are given in papers [14-15].

The generalized Fermi function (GFF) [8,14-15] is a simple function with a minimal number of parameters, suitable for X ray line profile (XRLP) global approximation based on minimization methods and it is defined by

$$h(s) = \frac{A}{e^{a(s-c)} + e^{-b(s-c)}}, \qquad (13)$$

where *A, a, b, c* are unknown parameters. The values *A, c* describe the amplitude and the position of the XRLP, *a, b* control its shape. For our analysis the most important properties of the GFF are;

(i) the integral width of experimental XRLP**,** $\delta_h(a,b)$ has the following form

$$\delta_h(a,b)=\frac{\pi}{(a^a b^b)^{1/(a+b)}\cos\left(\frac{\pi}{2}\frac{a-b}{a+b}\right)} \qquad (14)$$

(ii) by taking into account relations (10-11,13) the magnitude of *F(L)* function has the following form

$$|F(L)|=\frac{A_h\rho_g}{A_g\rho_h}\sqrt{\frac{\cos^2\alpha+\sinh^2\beta L}{\cos^2\gamma+\sinh^2\delta L}} \qquad (15)$$

where the arguments of trigonometric and hyperbolic functions are expressed by

$$q=\frac{a-b}{2},\ \rho=\frac{a+b}{2},\ \alpha=\frac{\pi q_g}{2\rho_g},$$

$$\beta=\frac{\pi^2}{\rho_g},\ \gamma=\frac{\pi q_h}{2\rho_h},\ \delta=\frac{\pi^2}{\rho_h}$$

The subscripts *g* and *h* refer to the instrumental and experimental XRLP

(iii) the integral width of the true XRLP sample can be expressed by the δ_f function

$$\delta_f(\rho_h,\rho_g)=\frac{\pi}{2\rho_h\cos\frac{\pi\rho_h}{2\rho_g}}\left(\cos\frac{\pi\rho_h}{\rho_g}+1\right). \qquad (16)$$

The data processing of the XRLP presented in the forth section is entirely based on the GFF approximation and its remarkable properties. The effective crystallite size, $D_{eff}(hkl)$ and the microstrain of the lattice $\langle\varepsilon^2\rangle_{hkl}$ were calculated using eqs. (13,15).

3. Experimental and data processing

3.1 Samples preparation

The gold catalysts were prepared by deposition – precipitation with urea (DP) and impregnation (IMP) methods. The oxide supports used for the preparation of gold catalysts were: Cr_2O_3, CeO_2, TiO_2, SiO_2, Al_2O_3 and ZrO_2,. All catalysts were prepared by DP method, except a sample of Au/SiO_2 which was prepared by IMP (labelled as Au/SiO_2-imp). For the catalysts preparation using DP method, 3g of oxide support was added to 75ml of aqueous solution containing $HAuCl_4$ (2×10^{-2}M) and ~1g urea. The suspension was vigorously stirred at 80°C for 16h. Urea decomposition led to a gradual rise of pH from 2 to 9. The solid was filtered and washed with distilled water. The operation was repeated 3 - 4 times, until no residual Cl was detected in the washing water. For Au/SiO_2-imp a solution containing 0.3g $HAuCl_4 \times 3H_2O$ in 4.5 ml distilled water was added to 3g SiO_2 and kept at room temperature for 24 h. All samples were dried in oven at 100°C for 16 h and calcinated in air at 300°C for 3h. The target loading of gold for catalysts was 5%wt.

3.2 Measurement methods

The transmission EXAFS measurements were carried out in the *4W1B* beamlines at Beijing Synchrotron Radiation Facilities (BSRF) operating at 50-80 mA and 2.2 GeV at room temperature. Due to the low concentration of active metal we used the florescence technique [16]. The beamline *4W1B* is an unfocussed monochromatic X-ray beam with 4 mrad of horizontal acceptance. The X-ray are monochromatized by a fixed exit *Si* double crystal monochromator.

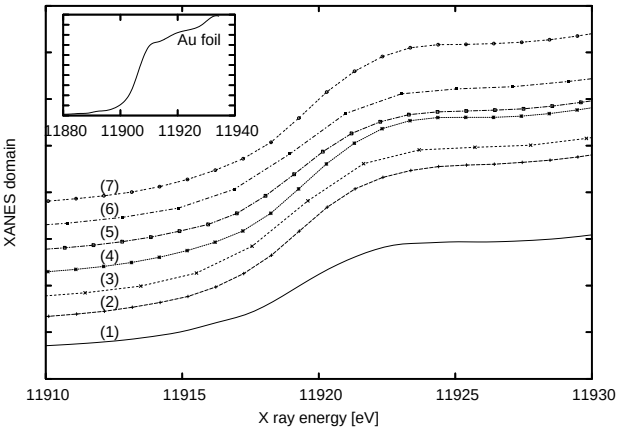

Fig. 1 XANES spectra of Au L_{III} edge, (1) – Au/Cr_2O_3, (2) - Au/CeO_2, (3) - Au/TiO_2, (4) - Au/SiO_2, (5) - Au/Al_2O_3, (6) - Au/SiO_2 imp, (7) - Au/ZrO_2

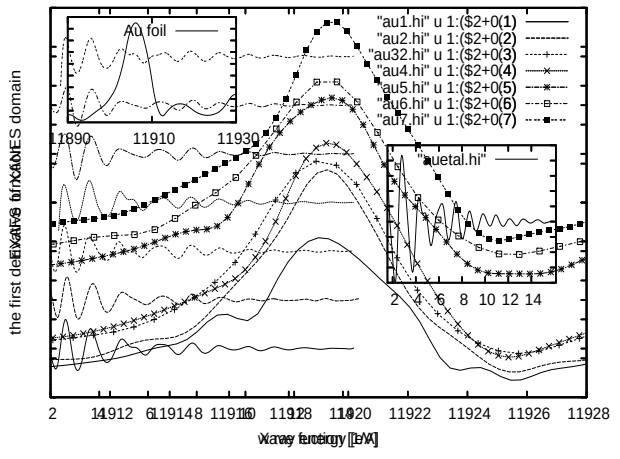

Fig. 2 The first derivative of XANES spectra for Au L_{III} edge.

The features of *4W1B* beamline are: energy range of *3.5-22 KeV*, energy resolution of *ΔE=0.5-2 eV* at *E =10KeV*, A gold foil with 99.98 % purity was used as a standard sample. Absorption coefficients of Au L_{III} edge were determined using a Si(111) double-crystal monochromator. Ionisation chambers monitored the X-ray intensities of incident and X ray florescence beams. Harmonics were rejected by monochromator detuning. The whole experimental system was controlled by a personal computer PS/2 for automatic data acquisition. All samples were ground to fine powder and homogeneously dispersed on Scotch tape. We used energy scanning range from *11788 eV* to *12914 eV* for measuring the absorption coefficients. The EXAFS analysis of the absorption coefficient was processed by the new computer codes EXAFS61 to EXAFS66 [17] from our own software library.

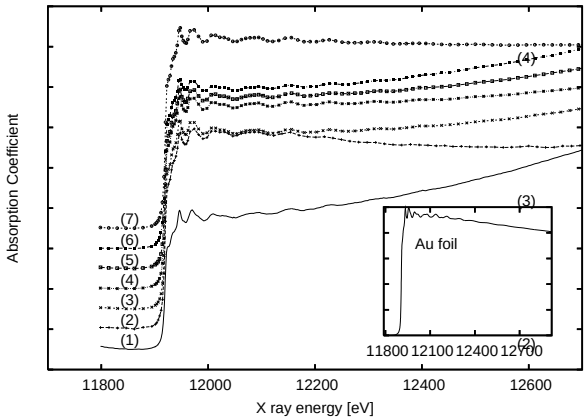

Fig. 3 The normalized absorption coefficients.

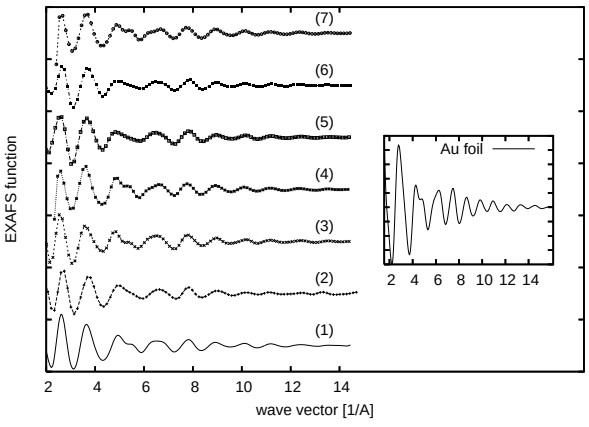

Fig. 4. The experimental EXAFS signals.

The X ray diffraction (XRD) measurements of the supported gold catalysts were collected using a horizontal powder diffractometer in Bragg-Brentano (BB) geometry on Dron 2 set up controlled by PC, having the Cu K_α radiation filtered.

The wavelength of the incident ray for XRD experiments was 1.5406 Å. A NaI (Tl) detector was used and signals were amplified, fed to single channel analyser and read out by a computer. The standard sample for X ray diffraction measurements was a SiO_2 very well crystallized. The scanning scale, 2θ, ranges from 20^0 to 80^0. The Fourier transform of the XRLP (111), (200), (220) and (113) were processed with the computer code SIZE developed in Maple 10. It is the improved version of XRLINE [18], and XRLINE1 [19] computer programs. Its purpose is to show intermediate processing results in a graphic manner.

4. Results and discussion

4.1 XANES and EXAFS results

Fig. 1 shows X ray Absorption Near Edge Structure (XANES) spectra for Au L_{III} edge investigated of the nanostructured gold catalysts as well as Au foil standard sample for energy calibration. The value of the threshold energy was taken as the position of maximum value for the first derivative of XANES spectra using the "bell" spline function technique [19]. The true positions of the Au L_{III} edge are illustrated in Fig. 2. The threshold energies of the investigated samples and their uncertainties are given in the forth and fifth columns of Table 1.

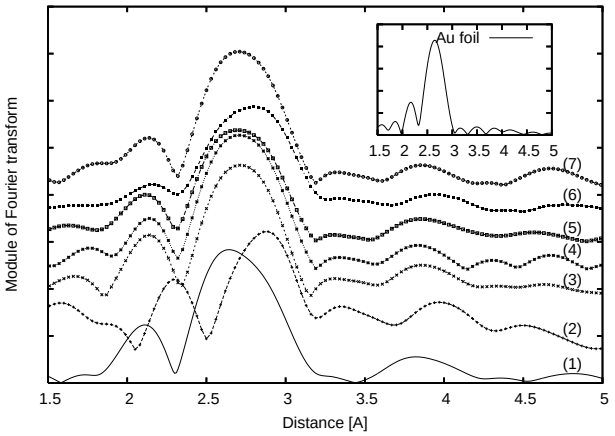

Fig. 5. The Fourier transforms magnitude of the EXAFS spectra.

The investigated samples from Table 1 have about the same value of threshold energy as the Au L_{III} edge, but their positions are shifted to higher energy compared with the binding energy, E_0=11919 eV, of the standard gold foil. This feature is due to the strong electronic interaction of the gold nanocrystallites surrounded by oxide supports.

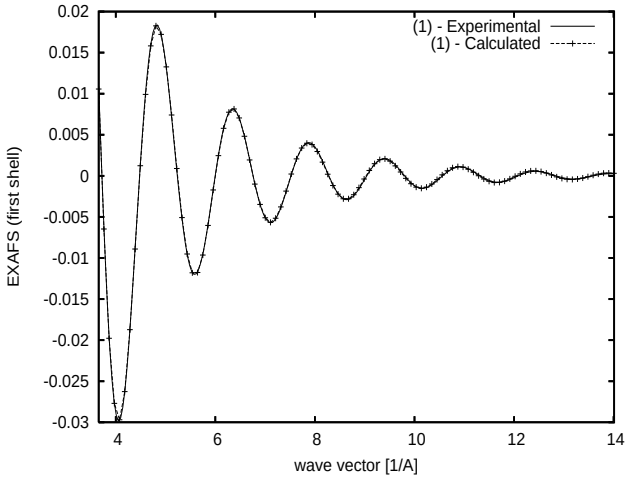

Fig. 6 The experimental and calculated EXAFS signals of the first shell for Au/Cr_2O_3.

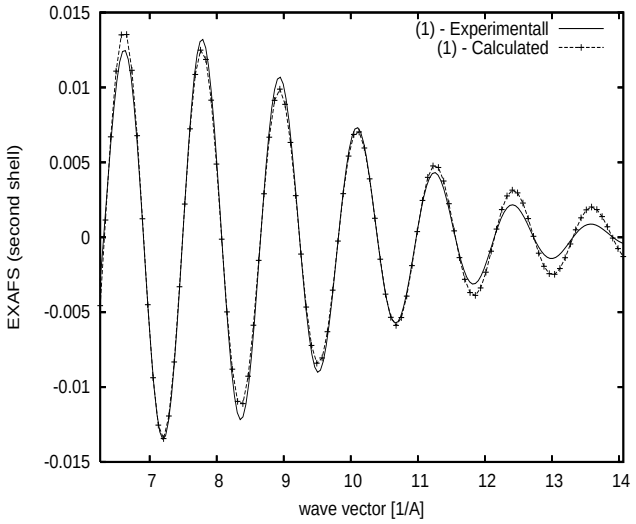

Fig.7 The experimental and calculated EXAFS signals of the second shell for Au/Cr_2O_3.

Fig. 3 shows the normalized absorption coefficients for the investigated supported gold catalysts as well as the gold foil as standard sample. The extraction of EXAFS signal is based on the threshold energy of Au L_{III} edge determination followed by background removal by pre-edge and after-edge base line fitting with different possible modelling functions, $\mu_0(k)$ and $\mu(k)$ evaluation. In accordance with eq. (1), the EXAFS signals were performed in the range 2×14 Å^{-1} and are presented in Fig. 4. In order to obtain the atomic distances distribution we calculated the RSF using Eq. (4). The mean Au-Au distances of the first and the second coordination shell for standard sample at room temperature are closed to values of $R_1 = 2.884$ Å and $R_2 = 4.079$ Å while the atom numbers are N_1=12 and N_2=6. By taking into account the classical algorithm dedicated for fast Fourier transform procedure we did not obtain reliable resolution for the RSF, due to spurious errors in spite of several types of filters used. To avoid this disadvantage we used the Filon algorithm for Fourier transform procedure [20] and the wave vector to the power of four. Based on this procedure the Fourier transforms of $k^4\chi(k)WF(k)$, performed in the range 1 - 5 Å, are shown in Fig. 5 for the investigated samples as well as for standard gold foil. In order to avoid wide peaks we considered $WF(k)=1$. The decreasing of the Fourier transform magnitude is the result of the reduced average coordination number. Each peak in $|\Phi(r)|$ is shifted from its true distance due to the phase shift function that is included in the EXAFS signal. We proceed by taking the inverse Fourier transform given by eq. (5) of the first neighbouring peak, and then extracting the amplitude function $A_j(k)$ and phase shift function $\delta(k)$ in accordance with eqs. (7-8). By using the Lavenberg-Marquard method to fit the eq.(6) on the experimental contribution for each coordination shell, we evaluated the interatomic distances, number of neighbours, edge position and mean free path parameters. Figs. 6 and 7 show calculated and experimental EXAFS functions χ_1(k) and χ_2(k) of the first shell as well as the second shell for the Au/Cr_2O_3 sample. In both cases the curves exhibit good similarities. Table 1 contains the best values of the local structure parameters. The errors given for the best-fit parameters have been estimated as ΔN, ΔR and ΔE_0.

Analysing the first coordination shell parameters we get a maximum increase in the radius of up to 6% for the Au/CeO_2 sample, while the average number of atoms decreases to 60% for Au/CeO_2 and to 16% for the Au/ZrO_2 sample. The parameters of the second coordination shell show an increase in the radius of up to 1.5%, while the number of atoms is diminished to only 41% for Au/CeO_2 sample. In both cases the comparison has been done under standard conditions. Therefore, we considered that this diminution of the number of atoms for both shell is due to a strong electron interaction between the gold nanoclusters and the surrounding metal oxides.

Table 1. The XAS parameters of the investigated samples.

The first coordination shell parameters				
The phase shift function parameters eq.(8)				
a_{-1}[Å]	a_0	a_1[Å^{-1}]	a_2[Å^2]	
0.0	-11.3293	-1.5172	0.0026	
The total amplitude parameters eq.(7)				
c_0[Å$^{2-c_3}$]	c_1[Å]	c_2[Å^{-2}]	c_3	
1.8955	0.3445	-0.0163	4.0271	
Sample	$N_1\pm\Delta N_1$	$R_1\pm\Delta R_1$[Å]	E_0[eV]	ΔE_0[eV]
Au/Cr_2O_3	7.24±0.08	2.82±0.06	11920.75	0.78
Au/CeO_2	4.77±0.09	3.05±0.05	11921.75	2.19
Au/TiO_2	8.43±0.05	2.89±0.04	11920.95	2.22
Au/SiO_2	9.92±0.06	2.86±0.07	11922.60	1.82
Au/Al_2O_3	7.35±0.07	2.84±0.05	11922.48	1.31
Au/SiO_2 -imp	6.43±0.05	2.86±0.06	11922.48	1.13
Au/ZrO_2	10.10±0.04	2.87±0.03	11922.60	2.06
The second coordination shell parameters				
The phase shift function parameters eq.(8)				
a_{-1}[Å]	a_0	a_1[Å^{-1}]	a_2[Å^{-2}]	
9.0510	-19.2964	-2.4796	-0.0124	
The total amplitude parameters eq. (7)				
c_0[Å$^{2-c_3}$]	c_1[Å]	c_2[Å^2]	c_3	
2.3792	-1.6864	0.0226	-9.3236	
Sample	$N_2\pm\Delta N_2$	$R_2\pm\Delta R_2$[Å]	E_0[eV]	ΔE_0[eV]
Au/Cr_2O_3	5.56±0.06	4.11±0.09	11920.75	0.49
Au/CeO_2	3.54±0.01	4.15±0.08	11921.75	0.09
Au/TiO_2	5.63±0.05	4.13±0.07	11920.95	0.25
Au/SiO_2	5.85±0.04	4.12±0.08	11922.60	0.52
Au/Al_2O_3	5.03±0.04	4.11±0.05	11922.48	0.36
Au/SiO_2 -imp	4.76±0.07	4.14±0.06	11922.48	0.05
Au/ZrO_2	5.67±0.05	4.08±0.07	11922.60	2.24

4.2 XRD results

Practically speaking, it is not easy to obtain accurate values of the crystallite size and microstrain without extreme care in experimental measurements and analysis of XRD data. The Fourier analysis of XRLP validity depends strongly on the magnitude and nature of the errors propagated in the data analysis. In paper [19] were treated three systematic errors: uncorrected constant background, truncation and the effect of the sampling for the observed profile at a finite number of points that appear in discrete Fourier analysis. In order to minimize propagation of these systematic errors, a global approximation of the XRLP is adopted instead of the discrete calculus. Therefore, herein the analysis of the diffraction line broadening in X-ray powder pattern was analytically calculated using the GFF facilities. The reason for this choice, as described in Section 2.2, was simplicity and mathematical elegance of the analytical Fourier transform magnitude and the integral width of the true XRLP given by eqs.(15) and (16). The robustness of the GFF approximation for the XRLP arises from possibility of using the analytical form of the Fourier transform instead of a numerical fast Fourier transform (FFT). It is well known that the validity of the numerical FFT depends on the filtering technique adopted [20]. In this way the validity of the nanostructural parameters are closely related to the accuracy of the Fourier transform magnitude of the true XRLP.

Here we processed only the profiles (111), (200), (220) and (113). Their experimental relative intensities with respect to 2θ values and Si powder as instrumental broadening effect are shown in Fig. 8. The next steps consist in background correction of XRLP by polynomial procedures and the determination of the best parameters of GFF distributions by nonlinear least squares fit. In order to determine the nanostructural parameters contained in eq. (12) we computed the Fourier transforms of the true XRLP and integral width using eqs. (15) and (16). In the previous section we have shown that the coordination shells radius of the investigated samples have similar values as the gold foil. This important result is strongly correlated with the positions of (111), (200), (220) and (113) XRLP from the experimental spectra contained in the last figures. Therefore, these results explain the metal oxide features of the investigated clusters despite of the strong deformation of the crystalline structure.

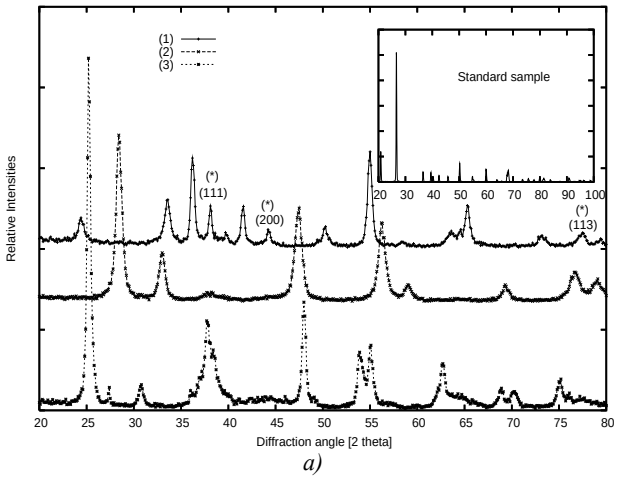

a)

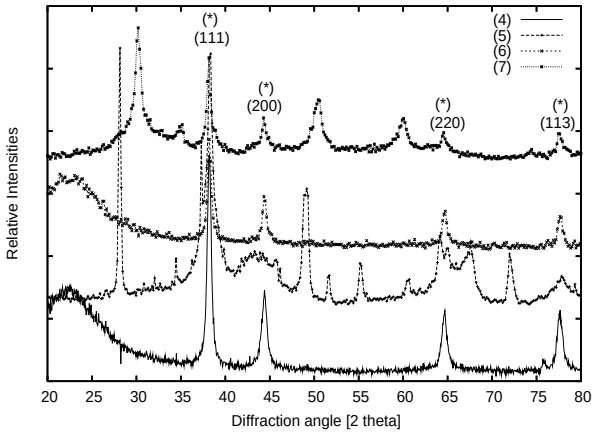

b)

Fig. 8 a), b) The relative intensities of experimental XRD line profiles. The XRLP of the gold nanoparticls are labelled by (*).

Hydrogen chemisorption, transmission electron microscopy, magnetization, electronic paramagnetic resonance and other methods could also be used to determine grain size of particles by taking into account a prior spherical form for the grains. By XRD method one can be obtain crystallite sizes that have different values for different crystallographic planes. There is a large difference between the grain size and the crystallite size due to the physical meaning of the two concepts. It is possible that the grains of the supported gold catalysts are built up of many Au crystallites.

The global structural parameters obtained for the investigated samples are summarized in Table 2. The size of the crystallites determined by eq. (12), corresponding to (111) (200), (220) and (113) planes, have values between 26 Å and 212 Å. This means that the geometry of the crystallites is not spherical. The microstrain parameter of the lattice can also be correlated with the effective crystallite size in the following way: the value of the effective crystallite size increases when the microstrain value decreases.

Table 2. The XRD parameters of the investigated samples.

Sample	Line	D_{eff}(Å)	D_{gen}[Å]	D_{arit}(Å)	D_{harm}(Å)	Microstrain x 10^{-5}	SFP [%]
Au/Cr_2O_3	(200)	180	152	145	145	0.103	0.35
Au/CeO_2	(111)	32	42	32	27	11.289	5.92
Au/TiO_2	(111)	53	38	38	40	8.102	5.73
Au/SiO_2	(111)	181	138	136	104	0.121	0.72
	(200)	94	97	90	72	1.512	1.96
	(220)	110	99	102	81	1.102	1.32
Au/Al_2O_3	(113)	27	26	21	25	12.101	5.97
Au/SiO_2 IMP	(111)	192	175	145	106	1.444	0.28
	(200)	150	123	119	91	1.741	0.70
	(220)	111	116	102	81	1.103	0.32
Au/ZrO_2	(111)	248	212	172	124	0.063	0.12
	(200)	154	142	127	98	0.825	0.54

5. Conclusions

In the present paper we have shown how, in addition to EXAFS analysis method and its specific advantages, XRD analysis can add more information to understanding the nanostructure of the gold nanoparticles surrounded by metal oxides. The main conclusions that can be drawn from these studies are:

(i) The decrease in the number of atoms from the first and the second coordination shells of Au in the investigated samples point out the existence of an electronic interaction between the gold nanoparticles and the surrounding supports

(ii) The local structure of the investigated systems shows a strong morphological modification of supported gold catalysts caused by the metal-support interaction. The morphological modifications of the local structure are responsible for the creation of active centres on the metal surface

(iii) In addition to these morphological modifications, the electronic structure might be modified with a large effect on catalytic activity

(iv) For XRLP analysis, a global approximation is applied rather than a numeric Fourier analysis. The former analysis is better than a numerical calculation because it can minimize the systematic errors that could appear in the traditional Fourier analysis.

(v) Our numerical results show that by using the GFF distribution we can successfully obtain reliable global nanostructural parameters.

Acknowledgements

The authors are grateful to BSRF for the beam time and to Dr. Hu Tiandou, Dr. Yie Yaning and Dr. Liu Tao for their technical assistance in EXAFS measurements. The author (N. A.) is also indebted to Professors Chen Hesheng, director of Institute of High Energy Physics and Fang Shouxian, director of BEPC National Lab., for their hospitality during his stage in IHEP. This work is the result of the Scientific Cooperation Agreement between our institutes. This work was supported by the research programme of Romanian Ministry of Education and Research by Grant CNCSIS 1484/2006.

References

[1] M. Haruta, Cattech **6**, 102 (2002).
[2] G. C. Bond, D. T. Thompson, Catal. Rev. - Sci. Eng., **41** 319 (1999).
[3] A. C. Gluhoi, M. A. P. Dekkers, B.E. Nieuwenhuys, J. Catal. **219**, 197 (2003).
[4] R. Grisel, K. Weststrate, A. Gluhoi, B.E. Nieuwenhuys, Gold Bulletin **35/2,** 45 (2002).
[5] N. Aldea, B. Barz, F. Aldea, J. Optoelectron. Adv. Mater. **9**(3), 651 (2007).
[6] N. Aldea, P. Marginean, V. Rednic, S. Pintea, B. Barz, A. Gluhoi, B. E. Nieuwenhuys, Xie, Yaning, F. Aldea, M. Neumann, J. Optoelectron. Adv. Mater. **9**(5), 1555 (2007).
[7] N. Aldea, B. Barz, S. Pintea, F. Matei, J. Optoelectron. Adv. Mater. **9**(10), 3293 (2007).
[8] N. Aldea, A. Gluhoi, P. Marginean, C. Cosma, X. Yaning, Spect. Acta A, Part B **455** 997-1008, (2000).
[9] A. G. McKale, B.W. Veal, A.P. Paulikas, S.K. Chan, G.S. Knapp, J. Am. Chem. Soc. **110**, 3763 (1988).
[10] S. P. Cramer, K.O. Hodgson, Prog. Inorg. Chem. **25**, 1 (1979)
[11] R. A. Scott, Methods Enzymol. **117**, 414 (1985).
[12] P. J. Ellis, H. C. Freeman, J.Synchrotron Rad. **2**, 190 (1995).
[13] F. W. Lytle, D. E. Sayers, E. A. Stern, Physica B, **158**, 701,(1989).
[14] N. Aldea, B. Barz, T. D. Silipas, F. Aldea, Z. Wu, J. Optoelectron. Adv. Mat. **7**(6), 3093 (2005).
[15] N. Aldea, B. Barz, A.C. Gluhoi, P. Marginean, X. Yaning, H. Tiandou, L. Tao,Z. Wu , Zhonghu, Wu, J. Optoelectron. Adv. Mat. **6**(4), 1287 (2004).
[16] B.S.R.F. Activity Report 2002, Bijing Electron Positron Collider National Laboratory.
[17] N. Aldea, E. Indrea, Comput. Phys. Commun. **60**, 145 (1990).
[18] N. Aldea, E. Indrea, Comput. Phys. Commun. **60**, 155 (1990).
[19] N. Aldea, R. Zapotinschi, C Cosma, Fresenius, J. Anal.Chem. **355**, 367 (1995).
[20] R. A. Young, R. J. Gerdes, A.J.C. Wilson, Acta Cryst. **22**, 155 (1967).
[21] J. S. Walker, Fast Fourier Transform*,* Second Edition, CRC Boca Raton, New York London, Tokyo, 1997.

* Corresponding author: *On leave from National Institute for Research and Development of Isotopic and Molecular Technologies, Cluj-Napoca, Romania
**naldea@itim-cj.ro